*applied sciences*

MDPI

*Article*

# Weak Molecular Signal Detection Mechanism Based on Cavity Plasmon

**Geng-Hao Chen * and Ye-Qi Zhang**

School of Mathematics and Physics, North China Electric Power University, Beijing 102206, China; yqzhang@ncepu.edu.cn
* Correspondence: 120232209094@ncepu.edu.cn

**Abstract**

Optical interrogation of weak infrared molecular signatures from hazardous small molecules is important for environmental monitoring and industrial safety. However, these weak molecular responses are often difficult to distinguish using conventional far-field spectroscopy. Here, we theoretically investigate an Ag metal–insulator–metal (MIM) nanocavity as a cavity-length-engineered plasmonic platform for molecular resonance-plasmon coupling. The molecular response is incorporated through an effective-medium dielectric model for a surface-confined molecular population within the 1 nm nanogap. By tuning the cavity length, the bare cavity plasmon resonance can be matched to a selected infrared-active molecular resonance, converting weak molecular absorption responses into a finite-contrast spectral splitting in the simulated spectrum. $SO_2$, $COCl_2$, and $H_2O$ are first investigated as representative systems, with optimized cavity lengths of 545, 404, and 190 nm, respectively. Using a unified 5% normalized dip-depth criterion, we identify the onset of spectral splitting and obtain local threshold molecular number densities of $4.47 \times 10^{24}$, $1.48 \times 10^{25}$, and $1.84 \times 10^{26}$ $m^{-3}$, respectively. The same cavity-matching and threshold-evaluation procedure is further applied to $NO_2$, $NH_3$, $PH_3$, HF, HCN, and $H_2S$. These results provide a comparative theoretical framework for molecule-specific cavity design in MIM nanocavities.

**Keywords:** plasmonic nanocavity; MIM nanocavity; infrared spectroscopy; spectral splitting; molecular resonance–plasmon coupling

## 1. Introduction

Reliable detection of small-molecule gases is needed in industrial safety monitoring, environmental monitoring, public health, and hazardous-gas early warning [1]. Since molecular spectra are closely related to molecular structure, different gases have their own characteristic absorption bands in the mid-infrared region [2]. Therefore, infrared spectroscopy is widely used for gas identification and molecular spectral analysis [3]. However, the optical responses of small molecules such as $SO_2$, $COCl_2$, $NO_2$, $NH_3$, $H_2S$, and HCN remain difficult to distinguish when the number of molecules within the optically active region is limited or when the molecules form an ultrathin surface-confined layer. Under these conditions, the molecular layer introduces only a weak dielectric perturbation, resulting in extremely small changes in the measured far-field spectrum [4].

Optical gas sensing techniques such as Fourier-transform infrared spectroscopy (FTIR), tunable diode laser absorption spectroscopy (TDLAS), and non-dispersive infrared spectroscopy (NDIR) identify gas species through vibrational absorption fingerprints [5–7].



Academic Editor: Paolo Prosposito

Received: 29 June 2026
Revised: 23 July 2026
Accepted: 25 July 2026
Published: 28 July 2026

At low ambient gas concentrations, however, the weak molecular absorption requires advanced optical setups such as long optical paths, multipass cells, strong light sources, and sensitive detectors [8]. Photoacoustic spectroscopy (PAS) converts absorbed optical energy into acoustic signals for gas detection, but its performance depends on light source intensity, acoustic cell design, and background noise [9,10].

Localized surface plasmon resonance (LSPR) sensors rely on refractive-index variations for label-free detection, but exhibit limited sensitivity to trace gases [11–13]. Surface-enhanced Raman scattering (SERS) and surface-enhanced infrared absorption (SEIRA) utilize plasmonic nanostructures that generate enhanced local electromagnetic fields [14–17]. Carbon-based SERS-active platforms have also been explored as alternatives to noble-metal substrates; for example, Keshavarz et al. reported nitrogen-doped graphite quantum nanostructures with a SERS enhancement factor of $3.2 \times 10^7$ for crystal violet at 100 nM [18]. Such platforms provide an alternative route for enhancing molecular vibrational signals [19]. However, most plasmonic enhancement techniques involve detecting small changes in signal intensity, which are easily masked by noise and baseline drift [20]. Therefore, signal engineering can be introduced to enhance the contrast in the cavity spectrum and enable resolvable mode splitting [21].

Plasmonic nanocavities offer an effective platform to enhance molecular vibrational signals and to study the interaction between molecular vibrations and confined optical modes [22,23]. Among these structures, finite-length MIM nanocavities are particularly suitable for enhancing molecular vibrational signals. In this type of cavity, the cavity plasmon mode can be regarded as an SPP standing wave [24]. In a narrow-gap finite-length MIM nanocavity, SPP propagate along the gap. After being reflected at the two open ends, they form SPP standing waves.

This geometry also allows the resonance wavelength of the cavity to be adjusted over a wide range [25]. By changing the cavity length or gap width, the cavity plasmon resonance can be shifted from the visible region to the mid-infrared region [26,27]. Many molecular vibrational modes are located in this spectral region [28,29]. When molecular mode is nearly resonant with the cavity plasmon mode, the molecular polarization response can be strongly enhanced [30–33]. The enhanced polarization response can modify the dispersion relation of the cavity mode [34]. The interaction between the molecular resonance and the cavity-plasmon mode can produce an interference-induced absorption dip and spectral splitting [35,36]. If the detuning between the molecular spectra and the cavity mode is varied, anticrossing behavior may also appear. For example, CO molecules adsorbed in Ag MIM nanocavities have been reported to show clear coupling between C–O stretching vibrations and cavity plasmons. This coupling produces clear spectral splitting. It also amplifies the molecular signal by about 2000 times and reduces the observable detection limit to about 800 molecules [37]. In this way, the originally weak molecular vibrational response can appear as distinguishable spectral features. This mechanism differs significantly from conventional plasmonic sensing, which mainly tracks refractive-index changes.

We investigate molecular resonance–plasmon coupling for several small molecules in an Ag MIM nanocavity. By adjusting the cavity length, the bare cavity plasmon resonance can be brought close to the characteristic vibrational absorption bands of $SO_2$, $COCl_2$, and $H_2O$. We find that the corresponding optimized cavity lengths are approximately 545, 404, and 190 nm, respectively. To isolate the molecular contribution from the intrinsic cavity response, we compare the absorption spectra of the gas molecules alone, the bare MIM cavity, and the gas-loaded MIM cavity. In this way, absorption dips and spectral splitting induced by the coupling between molecular vibrations and the cavity plasmon mode can be identified. We define the numerical onset of finite-contrast spectral splitting as the lowest molecular loading for which the normalized dip depth reaches 5%. When the absorption

peak is nearly resonant with the cavity plasmon mode, molecular polarization noticeably modifies the cavity spectrum. Therefore, even weak molecular spectra can be used to resolve spectral splitting. The corresponding threshold molecular spacings are 60.7, 40.7, and 17.6 Å for $SO_2$, $COCl_2$, and $H_2O$, respectively. The same analysis is then applied to HCN, $H_2S$, HF, $NH_3$, $PH_3$, and $NO_2$. We further identify the trend in the optimized cavity length and splitting threshold for different molecular optical responses. Cavity-length tuning matches selected molecular resonances to the cavity-plasmon mode and converts weak absorption into resolvable spectral features in the simulations.

## 2. Materials and Methods

### 2.1. Numerical Model and Simulation Setup

Electromagnetic simulations were performed using the frequency-domain interface of COMSOL Multiphysics 6.2, based on the finite-element method. A two-dimensional Ag MIM nanocavity was constructed, consisting of two identical silver plates separated by a 1 nm wide dielectric gap. For nanogaps wider than approximately 0.5–1 nm, quantum tunneling effects are usually negligible, and classical electrodynamics remains applicable [38–40]. Therefore, this study uses a classical electromagnetic framework based on Maxwell's equations, in which the dispersive dielectric function of silver is described by the Drude model [41], $\epsilon(\omega) = \epsilon_\infty - {\omega_p}^2/\left(\omega^2 + i\gamma\omega\right)$, where $\epsilon_\infty = 4.04$ is the permittivity at infinite angular frequency, $\hbar\omega_p = 9.172$ eV is the bulk plasma frequency, and $\hbar\gamma = 0.0207$ eV is the electron collision frequency.

The cavity length can be varied from 179 nm to 783 nm. This allows the MIM cavity resonance to be close to the absorption peak of different gas molecules. Perfectly matched layers were applied to the outer boundaries of the computational domain. They were used to suppress artificial reflections from outgoing electromagnetic waves. The structure is excited by a normally incident plane wave propagating along the $x$ direction, with the electric field polarized along the $z$ direction, thereby exciting the transverse-magnetic cavity plasmon mode. The optical response of the molecules near their characteristic vibrational frequencies was described using a Lorentz oscillator model: $\epsilon = 1 + N\alpha/(1 - N\alpha/3) \approx 1 + N\alpha_e + N\beta_v/\left(1 - \omega^2/{\omega_0}^2 - i\gamma\omega/{\omega_0}^2\right)$ The dielectric model and all parameter definitions follow those given in Ref. [37].

To analyze the strong local electromagnetic field in the nanoscale gap region, a highly fine non-uniform grid was adopted in the simulation. The maximum element size in the 1 nm nanogap was set to 0.2 nm to capture the near-field variation in the plasmonic hotspot, while progressively coarser elements were used away from the gap to reduce the computational cost. The numerical stability of this mesh setting was examined by reducing the maximum gap-element size from 0.2 to 0.05 nm. The two meshes produced identical peak wavelengths and splitting widths, while across the coarsest and finest meshes, the total relative variation was only 0.010116%. The corresponding mesh-refinement analysis is provided in Section S6 of the Supplementary Materials.

### 2.2. Spectral Analysis and Coupling Criterion

For each type of molecule, changes in molecular density affect the total coupling strength between the molecular vibration and the cavity plasmon mode. As the molecular density increases, the collective polarization response becomes stronger, and the hybridization between the molecular vibrational mode and the cavity plasmon mode becomes more pronounced. Therefore, the depth of the absorption dip and the spacing between the split peaks can be used as important spectral indicators of the coupling strength.

We use a simple quantitative criterion. We consider spectral splitting resolvable only when the depth of the absorption dip exceeds 5% of the average intensity of the

two adjacent split peaks. This criterion applies to all molecular systems studied in this work. We define the molecular density at which this criterion is first satisfied as the threshold molecular density, $N_{th}$. Here, the 5% normalized dip-depth criterion is used as an operational numerical definition of the onset of a finite-contrast spectral doublet in the noise-free simulated spectra. It is not intended to represent an instrument-specific detection limit. The dependence of the extracted threshold on this criterion was further examined using dip-depth values of 10% and 15%, as summarized in Table S3 of the Supporting Materials.

When the molecular density is below $N_{th}$, the influence of molecular vibrations on the cavity spectrum remains weak. In this case, the spectrum usually shows only slight distortion rather than clear and resolvable mode splitting.

The molecular-loading factor is denoted by $\rho$, while $N$ represents the molecular number density. The reference density is defined as $N_0 = N_A/V_m = 2.69 \times 10^{25}$ m$^{-3}$, where $V_m$ is the ideal-gas molar volume at 273.15 K and 1 atm. These conditions are used only to define $N_0$. The molecular number density and equivalent intermolecular distance are calculated as $N(\rho) = \rho^3 N_0, d_{eq}(\rho) = N(\rho)^{-1/3} = \frac{d_0}{\rho}$, where $d_0 = 3.34$ nm. The molecules are treated as a spatially homogeneous effective dielectric within the 1 nm nanogap. The resulting density represents a local effective molecular loading rather than the concentration of an equilibrium free gas. The complete concentration conversion and a detailed derivation of the conversions from $\rho$ to $N_{th}$, $d_{eq}$ and $c_{th}$ are provided in Section S1 of the Supplementary Materials. The present Lorentz model provides an initial effective-medium description and does not explicitly account for gas-phase environmental effects or adsorption-induced changes in molecular properties.

## 3. Results and Discussion

### 3.1. Tunable Resonance in Ag MIM Nanocavities

To study the influence of the cavity geometry on the optical response, an exposed Ag MIM nanocavity was analyzed first. In the gap range of less than 2 nm, the optical mode mainly originates from strongly localized surface plasmons, which form a standing wave-like distribution between metal interfaces [24], thereby achieving spectral tuning related to the geometry.

Figure 1 presents the absorption spectra of the bare Ag MIM nanocavity. It can be seen that in each spectrum, there exists a major resonance peak, which corresponds to the fundamental mode transverse magnetic mode, namely $TM_{10}$, while the higher-order modes are distributed in the shorter wavelength region, mainly below 2000 nm. As the cavity length increases from 190 nm to 545 nm, the resonant wavelength undergoes a continuous redshift, moving from approximately 2500 nm to approximately 7500 nm, basically covering the mid-infrared spectral range. This indicates that the structure can achieve spectral matching between cavity resonance and absorption peak by adjusting the cavity length. Meanwhile, the overall resonance intensity under different cavity lengths remains stable, indicating that the fundamental mode plasmon mode can be effectively excited. The cavity lengths selected in this paper are 190 nm, 277 nm, 404 nm and 545 nm. As the vibration frequency of the target molecule decreases, the required cavity length gradually increases, which also reflects the dependence of plasmon resonance on geometric dimensions.

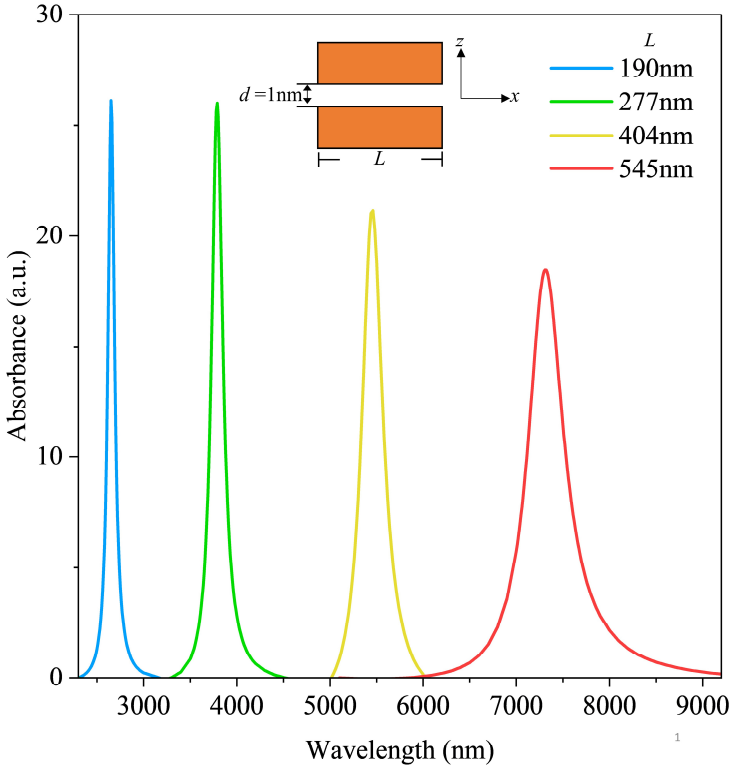


**Figure 1.** Calculated absorption spectra of bare Ag MIM nanocavities with a fixed gap width of $d = 1$ nm under different cavity lengths $L = 190,\ 277,\ 404,$ and 545 nm.

### *3.2. Molecular Vibration–Cavity Coupling and Spectral Splitting*

When the resonant frequency of the cavity is close to the resonance frequency of the molecule, the strong electromagnetic constraints in the nanoscale gap will enhance the interaction between the light field and the molecule. In this case, molecular polarization is no longer merely manifested as a very weak disturbance, but will have a significant impact on the cavity spectrum. The absorption valley will gradually widen, the resonance morphology will be distorted, and as the hybridization between the cavity plasmon mode and fundamental vibrations of molecule intensifies, mode splitting will further occur in the spectrum.

To evaluate this effect, the cavity lengths were adjusted based on the scale relationship established in Section 3.1. Eventually, the optimized cavity lengths for $H_2O$, $COCl_2$, and $SO_2$ were obtained as 190 nm, 404 nm, and 545 nm, respectively. The gap width was fixed at $d = 1$ nm, and all simulations were carried out within the same two-dimensional frame.

The spectral splitting is quantified using the 5% dip-depth criterion defined in Section 2.2. The evolution of spectral features is tracked as a function of the molecular number density $N$. The corresponding threshold $N_{th}$ defines the transition from weak perturbation to resolvable mode splitting for each molecular system.

### *3.3. $SO_2$ as a Representative System*

$SO_2$ molecules are first investigated to illustrate the density-dependent evolution of cavity–plasmonic spectral features. The cavity length is set to $L = 545$ nm to match the asymmetric stretching vibration mode of $SO_2$. Figure 2 shows the absorption spectrum of $SO_2$.

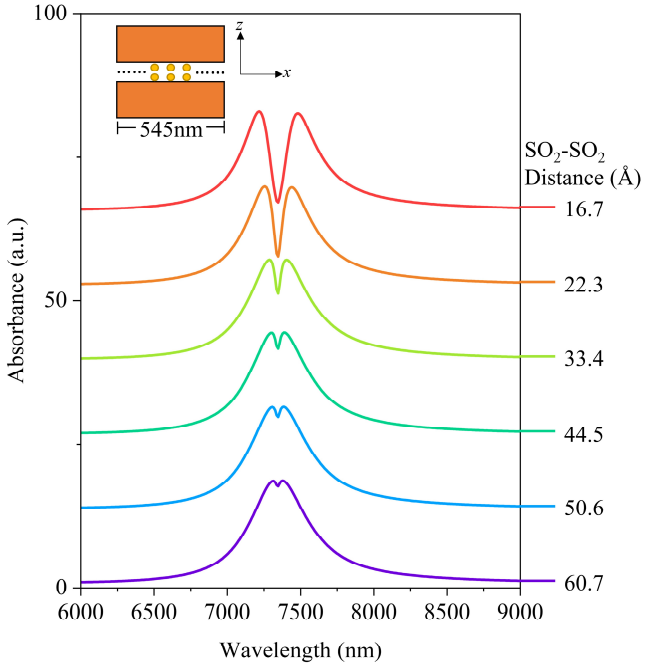


**Figure 2.** Calculated absorption spectra of $SO_2$ molecules in an Ag MIM nanocavity with gap width $d = 1$ nm and cavity length $L = 545$ nm. The spectra correspond to different intermolecular spacings of 60.7, 50.6, 44.5, 33.4, 22.3, and 16.7 Å.

Figure 2 shows the spectral evolution with decreasing intermolecular spacing. We can observe a split near the resonance center when the spacing is 60.7 Å. This marks the onset of measurable coupling between the cavity mode and the molecular asymmetric stretching mode. When the spacing is further reduced to 22.3 Å and 16.7 Å., the dip becomes deeper. Results show a continuous evolution from a weakly perturbed single-resonance regime to a hybridized mode-splitting regime with increasing molecular density.

### *3.4. $COCl_2$ and $H_2O$ Molecules*

Similar coupling behavior is also observed for $COCl_2$ and $H_2O$ molecules, as shown in Figure 3.

In Figure 3a, when the $COCl_2$ intermolecular spacing is large, the absorption spectrum mainly consists of a single resonance peak. As the spacing decreases, this peak gradually splits. The spectrum finally develops into a clear split structure. At 40.7 Å, a weak dip starts to appear near the resonance center. We regard this feature as the onset of spectral splitting associated with coupling between the cavity mode and the selected C=O stretching mode. With further reduction to 30.4 Å, a clearly resolved double-peak structure forms, and the mode separation increases.

The $H_2O$ molecules were analyzed using the same analytical method, and the corresponding spectral evolution is shown in Figure 3b. Similar to the changing trends of $SO_2$ and $COCl_2$, when the molecular spacing of $H_2O$ decreases to 17.6 Å, distinguishable spectral splitting features begin to appear at the resonance center. When the spacing is further as $d_{eq}$ decreases 11.1 Å, a more distinct and clearer pattern splitting profile can be observed. The threshold spacing of the $H_2O$ system was determined to be 17.6 Å, which is lower than the threshold spacing of 60.7 Å for $SO_2$ and 40.7 Å for $COCl_2$.

As shown in Figures 2 and 3, these three gaseous molecules all exhibit distinguishable plasmonic splitting at specific molecular spacings, but the corresponding threshold spacings and splitting amplitudes vary depending on the type of molecule. The selected resonance frequency primarily determines the cavity length required for resonance match-

ing, whereas the threshold also depends on the molecule-specific Lorentz parameters and the corresponding cavity-matching condition.

For $SO_2$, $COCl_2$ and $H_2O$, the optimized cavity lengths were 545 nm, 404 nm and 190 nm respectively. Under the same cavity mode and gap width, the matched cavity length generally decreases as the selected molecular vibrational frequency increases. That is to say, the higher the vibration frequency, the shorter the required cavity length. Under near-resonant conditions, the relation $\Delta\lambda \propto \sqrt{N\beta_v}$ reported in Ref. [37] indicates that a smaller equivalent intermolecular spacing, $d_{eq} = N^{-1/3}$, corresponds to a higher molecular number density and generally produces a larger spectral splitting. In the present model, the molecule-specific response is described by the Lorentz parameters, particularly $\beta_v$. Therefore, with each molecule evaluated at its matched cavity length, the calculated threshold reflects both the properties of the selected vibrational mode and the corresponding cavity-matching condition.

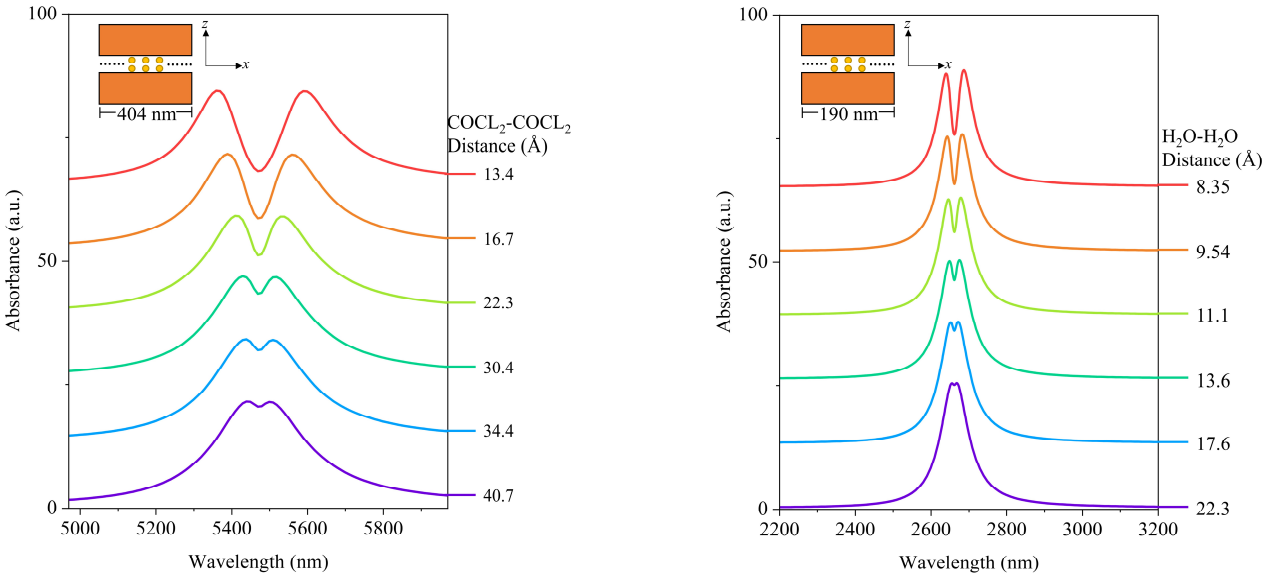


**Figure 3.** (**a**) Absorption spectra of $COCl_2$ molecules in an Ag MIM nanocavity with gap width $d = 1$ nm and cavity length $L = 404$ nm. The $COCl_2$ molecular spacings indicated in the legend are 40.7, 34.4, 30.4, 22.3, 16.7, and 13.4 Å. (**b**) Absorption spectra of $H_2O$ molecules in an Ag MIM nanocavity with gap width $d = 1$ nm and cavity length $L = 190$ nm. The $H_2O$ molecular spacings indicated in the legend are 22.3, 17.6, 13.6, 11.1, 9.54, and 8.35 Å.

### *3.5. Generalization to Multiple Gas Molecules*

The cavity length was optimized separately for the selected vibrational resonance of each additional molecular species, including HCN, $H_2S$, HF, $NH_3$, $PH_3$, and $NO_2$. The corresponding spectral responses were simulated under the same simulation conditions. Finally, the optimized cavity length, critical intermolecular distance, and extracted threshold density $N_{th}$ for each molecule are summarized in Table 1.

Due to differences in the response wavelength of these molecular species and their coupling efficiencies with the confined cavity field, different molecules exhibit distinct spectral behaviors. $SO_2$ and $NO_2$ show more efficient interaction with the cavity field because of their strong infrared-active molecular spectra, resulting in lower threshold densities. In contrast, HCN and $H_2S$ show weaker or more distributed optical responses, leading to reduced coupling efficiency and higher $N_{th}$ values.

**Table 1.** Summary of optimized cavity lengths $L$, corresponding cavity resonance wavelengths $\lambda_c$, threshold molecular number densities $N_{th}$, and equivalent intermolecular distances $d_{eq}$ for different gas molecules.

| Molecule | $L$ (nm) | $\lambda_c$ (nm) | $N_{th}$ ($m^{-3}$) | $d_{eq}$ (Å) |
|---|---|---|---|---|
| $SO_2$ | 545 | 7350 | $4.47 \times 10^{24}$ | 60.7 |
| $NO_2$ | 458 | 6184 | $9.22 \times 10^{24}$ | 47.7 |
| $COCl_2$ | 404 | 5473 | $1.48 \times 10^{25}$ | 40.7 |
| $NH_3$ | 783 | 10526 | $2.69 \times 10^{25}$ | 33.4 |
| $PH_3$ | 314 | 4297 | $6.61 \times 10^{25}$ | 24.7 |
| HF | 179 | 2525 | $9.07 \times 10^{25}$ | 22.3 |
| $H_2O$ | 190 | 2662 | $1.84 \times 10^{26}$ | 17.6 |
| HCN | 349 | 4769 | $1.85 \times 10^{27}$ | 8.15 |
| $H_2S$ | 277 | 3808 | $2.21 \times 10^{27}$ | 7.68 |

**Note**: $N_{th}$ denotes the threshold molecular number density for the onset of spectral splitting; $\lambda_c$ denotes the cavity resonance wavelength matched to the molecular spectra; $d_{eq}$ represents the equivalent intermolecular distance.

Detuning between the selected molecular resonance and the bare cavity-plasmon resonance also affects the degree of mode hybridization. Increasing detuning weakens mode hybridization and would generally require a higher molecular loading to satisfy the same dip-depth criterion. The corresponding cavity-length-dependent detuning behavior is illustrated and discussed in Figure S2 of the Supplementary Materials. In addition to cavity-length-induced detuning, changes in molecular concentration can also shift the cavity-plasmon resonance and modify the detuning condition. The resulting density-dependent cavity redshift and spectral-weight redistribution are discussed in detail in Section S5 of the Supplementary Materials. The systematic comparison of these parameters for each molecular species listed in Table 1 is summarized in the Supplementary Materials. The complete results, including spectral evolutions and threshold calculations, are provided in Supplementary Materials Figure S1 and Tables S2 and S3.

The calculated thresholds show an overall inverse trend with the molecular $\beta_v$ values. HCN and $H_2S$, which have particularly small $\beta_v$ values, require the highest molecular number densities; in contrast, modes with larger $\beta_v$ generally satisfy the spectral criterion at lower densities. However, the threshold ordering is not determined by $\beta_v$ alone, because the resonance frequency, damping rate, and corresponding cavity-matching condition also vary among the molecular systems.

The model describes an idealized, noise-free molecular effective medium in a 1 nm MIM nanogap. It does not include adsorption, mixture interference, pressure- or temperature-dependent effects, fabrication variability, or instrumental noise and resolution. The reported $N_{th}$ values are therefore numerical thresholds for the onset of spectral splitting rather than experimentally calibrated detection limits. Direct experimental validation remains necessary.

## 4. Conclusions

In conclusion, we have numerically investigated molecular resonance–plasmon coupling in an Ag MIM nanocavity by matching the cavity resonance to selected infrared-active molecular modes. Changing the cavity length $L$ shifts the MIM cavity resonance close to a selected infrared-active molecular resonance. As the cavity resonance approaches the molecular absorption spectrum, the weak molecular signal starts to emerge as a spectral splitting. Once the molecular density reaches the threshold value $N_{th}$, finite-contrast spectral splitting in the simulated spectrum appears in the absorption spectrum. Based on this approach, we determined the threshold molecular density $N_{th}$, the intermolecular spacing $d_{eq}$ required for spectral splitting, and the corresponding cavity length $L$ and resonance

wavelength $\lambda_c$ of the MIM cavity. Increasing the molecular density makes the split peaks deeper and broadens the splitting. This framework may support the molecule-specific design of MIM nanocavities and provide a basis for future experimental investigations of infrared molecular resonance–plasmon coupling.

**Supplementary Materials:** The following supporting information can be downloaded at: https://www.mdpi.com/article/10.3390/app16157494/s1.

**Author Contributions:** Conceptualization, G.-H.C.; Methodology, G.-H.C.; Software, G.-H.C.; Validation, G.-H.C.; Formal analysis, G.-H.C.; Investigation, G.-H.C.; Resources, Y.-Q.Z.; Data curation, G.-H.C.; Writing—original draft, G.-H.C.; Writing—review & editing, Y.-Q.Z.; Visualization, G.-H.C.; Supervision, Y.-Q.Z.; Project administration, Y.-Q.Z.; Funding acquisition, Y.-Q.Z. All authors have read and agreed to the published version of the manuscript.

**Funding:** This research was funded by National Natural Science Foundation of China, grant number 11805065.

**Institutional Review Board Statement:** Not applicable.

**Informed Consent Statement:** Not applicable.

**Data Availability Statement:** The data presented in this study are available from the corresponding author upon reasonable request.

**Acknowledgments:** During the preparation of this manuscript, ChatGPT (OpenAI, GPT-5.5) was used solely for language polishing. The authors have reviewed and edited the output and take full responsibility for the content of this publication.

**Conflicts of Interest:** The authors declare no conflicts of interest. The funders had no role in the design of the study; in the collection, analyses, or interpretation of data; in the writing of the manuscript; or in the decision to publish the results.

## Abbreviations

The following abbreviations are used in this manuscript:

| | |
|---|---|
| MIM | Metal–insulator–metal |
| FTIR | Fourier-transform infrared spectroscopy |
| TDLAS | Tunable diode laser absorption spectroscopy |
| NDIR | Non-dispersive infrared spectroscopy |
| PAS | Photoacoustic spectroscopy |
| LSPR | Localized surface plasmon resonance |
| SEIRA | Surface-enhanced infrared absorption spectroscopy |
| SERS | Surface-enhanced Raman scattering |

## References

1. Hodgkinson, J.; Tatam, R.P. Optical gas sensing: A review. *Meas. Sci. Technol.* **2013**, *24*, 012004. [CrossRef]
2. Gordon, I.E.; Rothman, L.S.; Hargreaves, R.J.; Hashemi, R.; Karlovets, E.V.; Skinner, F.M.; Conway, E.K.; Hill, C.; Kochanov, R.V.; Tan, Y.; et al. The HITRAN2020 molecular spectroscopic database. *J. Quant. Spectrosc. Radiat. Transf.* **2022**, *277*, 107949. [CrossRef]
3. Griffiths, P.R.; de Haseth, J.A. *Fourier Transform Infrared Spectrometry*, 2nd ed.; Wiley: Hoboken, NJ, USA, 2007.
4. Smith, B.C. *Fundamentals of Fourier Transform Infrared Spectroscopy*, 2nd ed.; CRC Press: Boca Raton, FL, USA, 2011.
5. Kreuzer, L.B. Ultralow gas concentration infrared absorption spectroscopy. *J. Appl. Phys.* **1971**, *42*, 2934–2943. [CrossRef]
6. Dinh, T.-V.; Choi, I.-Y.; Son, Y.-S.; Kim, J.-C. A review on non-dispersive infrared gas sensors: Improvement of sensor detection limit and interference correction. *Sens. Actuators B Chem.* **2016**, *231*, 529–538. [CrossRef]
7. Tan, X.; Zhang, H.; Li, J.; Wan, H.; Guo, Q.; Zhu, H.; Liu, H.; Yi, F. Non-dispersive infrared multi-gas sensing via nanoantenna integrated narrowband detectors. *Nat. Commun.* **2020**, *11*, 5245. [CrossRef] [PubMed]
8. Lin, S.; Chang, J.; Sun, J.; Xu, P. Improvement of the detection sensitivity for tunable diode laser absorption spectroscopy: A review. *Front. Phys.* **2022**, *10*, 853966. [CrossRef]
9. Patimisco, P.; Scamarcio, G.; Tittel, F.K.; Spagnolo, V. Quartz-enhanced photoacoustic spectroscopy: A review. *Sensors* **2014**, *14*, 6165–6206. [CrossRef] [PubMed]

10. Wijesinghe, D.R.; Zobair, M.A.; Esmaeelpour, M. A review on photoacoustic spectroscopy techniques for gas sensing. *Sensors* **2024**, *24*, 6577. [CrossRef] [PubMed]
11. Liedberg, B.; Nylander, C.; Lundström, I. Surface plasmon resonance for gas detection and biosensing. *Sens. Actuators* **1983**, *4*, 299–304. [CrossRef]
12. Homola, J.; Yee, S.S.; Gauglitz, G. Surface plasmon resonance sensors: Review. *Sens. Actuators B Chem.* **1999**, *54*, 3–15. [CrossRef]
13. Rodrigues, M.S.; Borges, J.; Lopes, C.; Pereira, R.M.S.; Vasilevskiy, M.I.; Vaz, F. Gas sensors based on localized surface plasmon resonances: Synthesis of oxide films with embedded metal nanoparticles, theory and simulation, and sensitivity enhancement strategies. *Appl. Sci.* **2021**, *11*, 5388. [CrossRef]
14. Ding, S.-Y.; Yi, J.; Li, J.-F.; Ren, B.; Wu, D.-Y.; Panneerselvam, R.; Tian, Z.-Q. Nanostructure-based plasmon-enhanced Raman spectroscopy for surface analysis of materials. *Nat. Rev. Mater.* **2016**, *1*, 16021. [CrossRef]
15. Langer, J.; Jimenez de Aberasturi, D.; Aizpurua, J.; Alvarez-Puebla, R.A.; Auguié, B.; Baumberg, J.J.; Bazan, G.C.; Bell, S.E.J.; Boisen, A.; Brolo, A.G.; et al. Present and future of surface-enhanced Raman scattering. *ACS Nano* **2020**, *14*, 28–117. [CrossRef] [PubMed]
16. Hartstein, A.; Kirtley, J.R.; Tsang, J.C. Enhancement of the infrared absorption from molecular monolayers with thin metal overlayers. *Phys. Rev. Lett.* **1980**, *45*, 201–204. [CrossRef]
17. Neubrech, F.; Huck, C.; Weber, K.; Pucci, A.; Giessen, H. Surface-enhanced infrared spectroscopy using resonant nanoantennas. *Chem. Rev.* **2017**, *117*, 5110–5145. [CrossRef] [PubMed]
18. Keshavarz, M.; Chowdhury, A.K.M.R.H.; Kassanos, P.; Tan, B.; Venkatakrishnan, K. Self-assembled N-doped Q-dot carbon nanostructures as a SERS-active biosensor with selective therapeutic functionality. *Sens. Actuators B Chem.* **2020**, *323*, 128703. [CrossRef]
19. Li, D.; Xu, C.; Xie, J.; Lee, C. Research progress in surface-enhanced infrared absorption spectroscopy: From performance optimization, sensing applications, to system integration. *Nanomaterials* **2023**, *13*, 2377. [CrossRef] [PubMed]
20. Neubrech, F.; Pucci, A.; Cornelius, T.W.; Karim, S.; García-Etxarri, A.; Aizpurua, J. Resonant plasmonic and vibrational coupling in a tailored nanoantenna for infrared detection. *Phys. Rev. Lett.* **2008**, *101*, 157403. [CrossRef] [PubMed]
21. Adato, R.; Aksu, S.; Altug, H. Engineering mid-infrared nanoantennas for surface enhanced infrared absorption spectroscopy. *Mater. Today* **2015**, *18*, 436–450. [CrossRef]
22. Huck, C.; Toma, A.; Neubrech, F.; Chirumamilla, M.; Vogt, J.; De Angelis, F.; Pucci, A. Gold nanoantennas on a pedestal for plasmonic enhancement in the infrared. *ACS Photonics* **2015**, *2*, 497–505. [CrossRef]
23. Rodrigo, D.; Limaj, O.; Janner, D.; Etezadi, D.; García de Abajo, F.J.; Pruneri, V.; Altug, H. Mid-infrared plasmonic biosensing with graphene. *Science* **2015**, *349*, 165–168. [CrossRef] [PubMed]
24. Yang, D.-J.; Ding, S.-J.; Ma, L.; Mu, Q.-X.; Wang, Q.-Q. SPP standing waves within plasmonic nanocavities. *Opt. Express* **2022**, *30*, 44055. [CrossRef] [PubMed]
25. Lassiter, J.B.; McGuire, F.; Mock, J.J.; Ciracì, C.; Hill, R.T.; Wiley, B.J.; Chilkoti, A.; Smith, D.R. Plasmonic waveguide modes of film-coupled metallic nanocubes. *Nano Lett.* **2013**, *13*, 5866–5872. [CrossRef] [PubMed]
26. Memmi, H.; Benson, O.; Sadofev, S.; Kalusniak, S. Strong coupling between surface plasmon polaritons and molecular vibrations. *Phys. Rev. Lett.* **2017**, *118*, 126802. [CrossRef] [PubMed]
27. Dunkelberger, A.D.; Spann, B.T.; Fears, K.P.; Simpkins, B.S.; Owrutsky, J.C. Modified relaxation dynamics and coherent energy exchange in coupled vibration-cavity polaritons. *Nat. Commun.* **2016**, *7*, 13504. [CrossRef] [PubMed]
28. Chikkaraddy, R.; de Nijs, B.; Benz, F.; Barrow, S.J.; Scherman, O.A.; Rosta, E.; Demetriadou, A.; Fox, P.; Hess, O.; Baumberg, J.J. Single-molecule strong coupling at room temperature in plasmonic nanocavities. *Nature* **2016**, *535*, 127–130. [CrossRef] [PubMed]
29. Chen, W.; Zhang, S.; Deng, Q.; Xu, H. Probing of sub-picometer vertical differential resolutions using cavity plasmons. *Nat. Commun.* **2018**, *9*, 801. [CrossRef] [PubMed]
30. Ciracì, C.; Hill, R.T.; Mock, J.J.; Urzhumov, Y.; Fernández-Domínguez, A.I.; Maier, S.A.; Pendry, J.B.; Chilkoti, A.; Smith, D.R. Probing the ultimate limits of plasmonic enhancement. *Science* **2012**, *337*, 1072–1074. [CrossRef] [PubMed]
31. Benz, F.; Schmidt, M.K.; Dreismann, A.; Chikkaraddy, R.; Zhang, Y.; Demetriadou, A.; Carnegie, C.; Ohadi, H.; de Nijs, B.; Esteban, R.; et al. Single-molecule optomechanics in picocavities. *Science* **2016**, *354*, 726–729. [CrossRef] [PubMed]
32. Chikkaraddy, R.; Xomalis, A.; Jakob, L.A.; Baumberg, J.J. Mid-infrared-perturbed molecular vibrational signatures in plasmonic nanocavities. *Light Sci. Appl.* **2022**, *11*, 19. [CrossRef] [PubMed]
33. Arul, R.; Benjamin-Grys, D.; Chikkaraddy, R.; Mueller, N.S.; Xomalis, A.; Miele, E.; Euser, T.G.; Baumberg, J.J. Giant mid-IR resonant coupling to molecular vibrations in sub-nm gaps of plasmonic multilayer metafilms. *Light Sci. Appl.* **2022**, *11*, 281. [CrossRef] [PubMed]
34. Xiang, B.; Ribeiro, R.F.; Du, M.; Chen, L.; Yang, Z.; Wang, J.; Yuen-Zhou, J.; Xiong, W. Intermolecular vibrational energy transfer enabled by microcavity strong light–matter coupling. *Science* **2020**, *368*, 665–667. [CrossRef] [PubMed]
35. Chandran, A.; Barnard, E.S.; White, J.S.; Brongersma, M.L. Metal-dielectric-metal surface plasmon-polariton resonators. *Phys. Rev. B* **2012**, *85*, 085416. [CrossRef]

36. Yang, D.J.; Zhang, S.; Im, S.J.; Wang, Q.Q.; Xu, H.; Gao, S. Analytical analysis of spectral sensitivity of plasmon resonances in a nanocavity. *Nanoscale* **2019**, *11*, 10977–10983. [CrossRef] [PubMed]
37. Yang, D.-J. Direct detection of ultraweak CO signal with cavity plasmon by resonant vibration–plasmon coupling. *Adv. Theory Simul.* **2020**, *3*, 2000146. [CrossRef]
38. Zuloaga, J.; Prodan, E.; Nordlander, P. Quantum description of the plasmon resonances of a nanoparticle dimer. *Nano Lett.* **2009**, *9*, 887–891. [CrossRef] [PubMed]
39. Esteban, R.; Borisov, A.G.; Nordlander, P.; Aizpurua, J. Bridging quantum and classical plasmonics with a quantum-corrected model. *Nat. Commun.* **2012**, *3*, 825. [CrossRef] [PubMed]
40. Scholl, J.A.; García-Etxarri, A.; Koh, A.L.; Dionne, J.A. Observation of quantum tunneling between two plasmonic nanoparticles. *Nano Lett.* **2013**, *13*, 564–569. [CrossRef] [PubMed]
41. Rakić, A.D.; Djurišić, A.B.; Elazar, J.M.; Majewski, M.L. Optical properties of metallic films for vertical-cavity optoelectronic devices. *Appl. Opt.* **1998**, *37*, 5271–5283. [CrossRef] [PubMed]